Quasistatic Strain Fields in Normally- and Tangentially-Loaded Elastomeric Rollers Under Impending Slip

Nehemiah Mork[a], Milosz K. Rajchel[a], Michael Varenberg[a], Antonia Antoniou[a] and Michael J. Leamy[a,*]

[a]*The Woodruff School of Mechanical Engineering, Georgia Institute of Technology, Atlanta, 30318, Georgia, USA*

ARTICLE INFO

Keywords:
Digital image correlation
Ncorr
Strain field
String model
Contact mechanics

ABSTRACT

Elastomeric rollers are important components in applications such as printing and roll-to-roll manufacturing. To gain insight into roller mechanics and provide a basis for further investigations into dynamic rolling problems where rolling instabilities and rolling friction arise, we employ a specially-designed apparatus to obtain displacement and strain fields via digital image correlation (DIC) under applied loads. We test loading scenarios leading to impending slip of an elastomeric roller, mounted on a steel hub, and in contact with a glass (rigid) substrate. We first examine strain fields under normal loading and compare them with the closest analytical predictions. We also analyze the strain fields under normal and tangential loading for which limited analytical predictions exist. For each loading scenario, we discuss the displacement and strain fields of the roller sidewall and contact interface. We implement a conceptual string model to demonstrate how stick and slip zones develop within the contact area as well as how memory effects arise during cyclic loading. This memory effect is then verified experimentally using the DIC strain fields. Additionally, we demonstrate a means for identifying the stick zone area between the roller and substrate using the experimentally-obtained displacement fields. We believe the apparatus, and the ability to obtain experimental displacement and strain fields, will prove valuable in understanding roller mechanics and associated instabilities.

1. Introduction

Rolling contact of tires or rollers against a rigid surface is common in numerous applications from aviation to roll-to-roll manufacturing. Under certain conditions instabilities, such as Schallamach waves [1–3], may be generated leading to roller degradation and misalignment. As a first step in fully understanding these conditions, in this paper we experimentally measure quasistatic fields under normal and tangential loading up to the point of impending slip.

The analysis of frictional contact goes back to the classical papers by Cattaneo [4] and Mindlin [5]. For two dimensional frictional contact problems involving tangential loading, Ciavarella [6, 7] assembled a procedure for generating pressure distribution and tractions in partial slip frictional contact problems of various geometries, including cylinders. While extensive literature into frictional contact problems exist, few analytical solutions of rolling contact problems [8] exist for relating applied loads to frictional forces, material displacements, and internal stresses [9, 10]. Furthermore, such solutions are valid for a limited number of geometries, loading cases, and constitutive behaviors [10, 11]. Popov presented an analytical solution to the normal loading case for frictionless contact of a deformable 2D roller attached to a rigid semicircular hub in contact with a flat rigid surface [9]. While this solution provides valuable insight into contact behavior, it is limited due to the absence of friction, and is only valid for strains along the contact interface. This method is also limited to cases where the thickness of the elastic layer is very small compared to the contact radius of the roller and the indentation depth is much smaller than the thickness of the elastomer layer. There is also the Hertzian contact solution of elastomeric rollers, but that solution lacks many geometric features that are significant in the development of the strain fields within a roller, mainly the rigid hub and contact with a rigid surface. Analytical expressions for the tangential strains in the contact patch are extremely limited, and to the best of the authors' knowledge, can only be found in half-plane and spherical contact problems [9, 12, 13].

In the absence of analytical contact solutions, finite element models have been used to extract fields for a given geometry, boundary conditions and material properties. Using such models, full deformation fields have been simulated to characterize contact between rolling elements [14–18]. A challenge arises for tangential loading since mechanical contact behavior and associated models (e.g., friction and elastic slip criteria) are material-dependent and still under development, and thus can greatly affect the reliability of predicted response quantities.

A complement to numerical simulations are experimentally-obtained strain fields using digital image correlation (DIC) [19]. For contact problems, DIC has been used to obtain displacement fields and to characterize tire vibrational response [20], measure traction [21], analyze stick-slip behavior [22], measure tangential stiffness [23, 24], and extract two-dimensional strain fields of the sidewall of a diametrically loaded cylinder [25]. However, a thorough DIC-based investigation of the effects of normal and tangential loading on the strain fields of an elastic rolling element in contact with a rigid surface has not yet been carried out. These fields become particularly important as one embarks on understanding instabilities under rolling contact during extreme path-tracking [26] and tire bursting [27].

---

*Corresponding author: michael.leamy@me.gatech.edu
ORCID(s):

Frictional contact problems, including frictional rolling, are found to generate a memory effect which can produce residual displacements and strains, which is of interest herein. This memory effect is noted by Jäger when analyzing two elastic half-planes in quasi-static contact under normal and tangential loading [28]. This memory effect, as well as stick and slip zone development, is further explained by Barber while analyzing quasi-static frictional contact problems of elastic half-planes under cyclic loading [29]. As for the case of elastomeric rollers in contact with a rigid substrate, they may undergo tangential displacements even under purely normal loading [30]. Previous research demonstrates that such systems posses a form of memory [31] that resides in the values of tangential displacements and strains within the stick zones [29, 32]. When the tangential load is first increased and then reduced, friction forces in the slip regions do not disappear and instead reverse, resulting in residual slip displacement and stress [31, 33]. The residual displacements and stresses become the initial conditions for material entering the contact region and thus introduce a memory effect. When friction is present during cyclic Hertzian contact between an elastic cylinder and a rigid plane, this memory effect eventually converges to a steady state after 3-5 cycles [34]. After repeated loading and unloading, the contact region forms slip zones near edges of the contact area which cycle back and forth between stick and slip. It is important to reveal these memory effects and thus account for residual displacement and strain.

String models enable tractable approximations and predictions of stress, stick and slip zones, and memory effects by simplifying the tire-hub and tire-contact interactions. The first string model for tire-hub interaction, presented in 1941 by Schlippe [36], uses a stretched string carcass representation. More specifically, the tire is simplified to a stretched spring connected to the hub by visco-elastic springs. Many variations to this model have since appeared, including frequency-domain models used to study tire harmonics [37]. String models of the tire contact interaction are of particular interest herein. The brush model is a well-known example used to predict tire-contact forces [38–40]. The tire or roller is first broken into discrete, independent sections which appear as bristles brushing the ground during rolling. During dynamic rolling, the contact area is decomposed into a leading stick region and trailing slip region. The size of the stick zone is determined by comparing the applied tangential force to the static friction capable of being supported by each bristle [41]. While appropriate for dynamic rolling, this decomposition is inaccurate for rollers under impending slip, where at a minimum two slip zones and a stick zone arise.

In this work we employ 2D DIC to measure displacement and strain fields along two planes of a constrained roller which is free to rotate but not translate. One plane is that of the contact area between the roller and rigid substrate and the other is the side wall of the elastomeric roller encased around the steel hub. We perform two loading cases: (1) purely normal loading relative to an unloaded roller and (2) tangential loading relative to the normally-loaded roller leading to the onset of gross slip. A string model is implemented to clearly describe how a strain memory effect arises in the contact area during cyclic loading. This memory effect is then demonstrated using experimental strain fields obtained during tangential loading and unloading. The same string model is also implemented to conceptually explain the development of stick and slip zones that develop in the contact region of the roller under static tangential loading. Lastly, we experimentally verify theoretical predictions of a decrease in stick zone area during increased tangential loading.

2. Experimental Protocol

To study roller deformation up to the onset of gross slip, we first impose normal loading followed by a torque-inducing tangential load. We apply both loading scenarios to an elastomeric roller in contact with a rigid glass substrate. Throughout loading we measure displacement and strain fields from the roller contact patch and sidewall using DIC. The experimental apparatus employed for loading and imaging of the roller is documented in detail in Ref. [35]. Figures 1 (a) - (c) present top and side views of the test setup with a roller in place. The elastomeric roller encases a rigid steel hub resting inside an aluminum housing. The steel hub is free to rotate, but not translate, about one plane and can be lifted or lowered by a lever. The lever setup is adjusted to ensure the normal contact occurs along the entire width of the roller. The glass substrate is attached to the top of the testing structure by linear rails to allow for smooth uniaxial translation. While generally the substrate can translate on the linear rails inducing rotation of the roller, for this work, we fix the substrate in order to explore impending slip. While we refer to the wheel as a roller throughout this work, we emphasize that this work analyzes quasistatic loading to the onset of gross slip and this is not a rolling contact scenario. It is important to note this distinction here since rolling develops quite different contact mechanics compared to a quasistatic loading scenario.

Two loads can be applied to the roller during testing. We apply a normal load by filling the empty vessel in Figs. 1 (a) and (c) with water. The vessel attaches to a lever which subsequently applies an upward normal load to the hub of the roller, thereby pressing it upwards against the rigid glass substrate. The second load is tangential to the roller hub. As displayed in Figs. 1 (b) and (c), a string wraps around each end of the roller hub and is tied to a rigid, threaded, steel rod. A single cord then runs from this threaded rod to a pulley and down to a second empty vessel. By filling this second vessel with water, the strings tension and act as a tangential force to the hub of the roller, ultimately initiating a torque on the roller. Figure 1 (d) presents a simplified model of the roller, applied loads, and viewing angles. We fill both water vessels at a constant rate of 18.5 mL/s, or equivalently, 0.18 N/s. The first water vessel applies a maximum normal load of 9.8 N (N_{max}). The second vessel applies a maximum tangential load of 8.8 N (T_{max}).

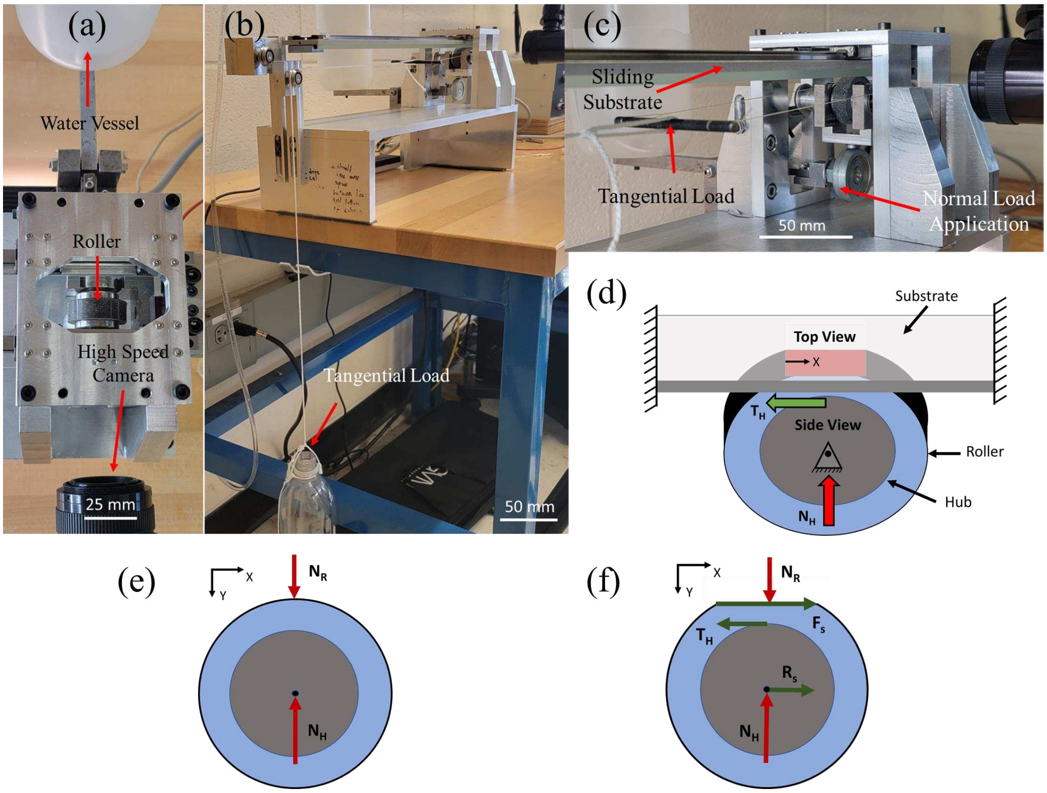

Figure 1: Experimental setup and loading scenarios. Additional details about the experimental setup can be found in Ref. [35]. (a) Top view of the roller imaged through a transparent glass (approximated as rigid) substrate. A high speed camera captures images along the side view of the roller as the load is applied. (b) Tangential load is applied to the roller hub by filling an empty vessel hanging off the table with water. (c) Normal load is applied by filling an empty vessel with water lifting a lever which in turn presses the roller against the rigid substrate. (d) Simplified schematic of loading scenarios and imaging views. The roller is pinned in place meaning it is free to rotate but not able to translate. (e) Normal loading diagram. (f) Tangential loading diagram.

The elastic roller placed around the steel hub has an outer diameter of 30 mm, an inner diameter of 20 mm, and a thickness of 10 mm in the axial direction. It is fabricated from Sylgard 184 PDMS and black paint. The PDMS preparation and curing protocol can be found in detail in Ref. [35]. After fabrication, the roller has an expected elastic modulus of 1.85 MPa and Poisson's ratio of 0.495 [35]. The sidewall and roller circumference are coated with a random speckle pattern to enable strain mapping. The speckles have an average diameter of 0.1 mm using gold, white, and green paint. Lastly, the roller is heat treated at 75 °C for an hour to cure the speckles to the roller surface.

As presented in Fig. 1 (d), we image both the roller contact patch as well as the roller sidewall. A Samsung Galaxy S21 Ultra phone camera images the contact patch from above through the clear glass substrate at a rate of 60 frames per second (FPS). A Chronos 14-1.1-34M high speed camera images the roller sidewall. The high speed camera is capable of achieving between 20 and 1069 FPS. For this work, since we only measure quasi-static strain fields, we image at a rate of 60 FPS to align with the phone camera. Image acquisition is timed with water flow to begin imaging when we initiate loading. The images are analyzed using the open-source in-house software Ncorr. Ncorr extracts the in-plane displacements from the unique speckling pattern on the roller surfaces and uses the displacement fields to obtain 2D strain fields [19].

Figures 1 (e) and (f) present free body diagrams of the two loading cases. We note here that the x, y, z coordinates throughout the paper are oriented such that they align circumferentially along contact area, normally to the contact area, and axially respectively. First, we investigate the resulting displacement and strain fields of the elastomeric roller under a purely normal load as depicted in Fig. 1 (e). The reference image for this test corresponds to the roller not yet in contact with the glass substrate (zero normal load applied). For this loading case the normal load (N_H) increases from 0 to $\mathrm{N_{max}}$. The hub experiences the applied normal force, N_H, causing the elastomeric roller to subsequently experience a reaction force against the glass substrate, N_R. We are not concerned with the induced friction forces from pure normal loading. In the second loading scenario we analyze the roller under a normal load as well as a tangential load that imposes a counterclockwise torque. The roller first undergoes a normal load equal to $\mathrm{N_{max}}$. The roller under this maximum normal load is the reference for the second loading scenario. A tangential load (T_H) is then applied to

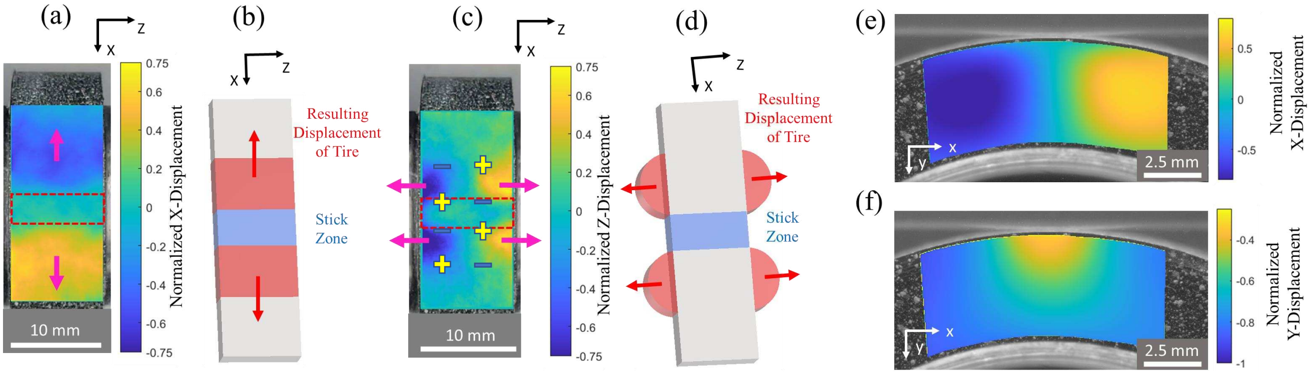

Figure 2: (a) Top view x-component of displacement (u) resulting from a normal load. The contact area is noted as a red dashed outline. (b) Simplified depiction for explaining the u displacement field. The blue region represents the stick zone and the red regions represents the deformed roller material on either side of the stick zone. (c) Top view z-component of displacement (w) resulting from a normal load. The positive and negatives slopes ($\partial w/\partial x$) are marked with "+" and "-" signs respectively. (d) Simplified depiction for explaining the w displacement field. (e) Sidewall normalized x-component of displacement (u). (f) Sidewall normalized y-component of displacement (v).

the hub of the roller and increases from 0 to $\mathrm{T}_{\max}$. In this case, the roller experiences both applied and reactive normal loads as well as the applied tangential force, T_H, and friction forces in the contact area (F_S). In both loading scenarios, when we analyze the images in Ncorr, we use a subset radius of 29 pixels (0.87 mm in top view and 0.29 mm in side view), a subset spacing of 2 pixels (0.06 mm in top view and 0.02 mm in side view), and a strain radius of 15 pixels (0.45 mm in top view and 0.15 mm in side view). The resulting strain fields are re-sized using the the *imresize* function in MATLAB such that the strain points correlate 1:1 with the pixels of the original image. All displacement and strain fields presented herein are an average of five different trials to aid in identifying any fluctuations between the different runs. The averaged strain fields are then normalized with respect to the average contact strain $\bar{\varepsilon}_n$ of the roller which is calculated using the applied force, elastic modulus of the roller, and the contact area. The normalization procedure is detailed in Appendix A.

3. Normal Loading

Figure 2 (a) displays the top view x-component of displacement (u) resulting from the applied normal load. This displacement field is normalized with respect to the point of maximum magnitude of displacement. In this work we consider the full contact region under normal loading to be a stick zone with no slip zones which is supported in previous studies to date [9–11]. This is expected since the elastic roller is largely incompressible with a much smaller small shear modulus than the rigid substrate resulting in a Dunders' bimaterial constant of essentially zero ($\beta = 0$) [42, 43]. A bimaterial constant of zero represents the two materials as elastically similar [44] resulting in a fully stuck contact area. The contact width under maximum normal load, $\mathrm{N}_{\max}$, is found to be 4.2 mm. As this normal load is applied, material points displace away from the contact area. Figure 2 (b) presents a depiction for this deformation during loading. The blue section in Fig. 2 (b) represents the stick zone and in this case contact area. As we increase the applied normal load, a larger arc length of the tire is pressed into contact with the rigid substrate increasing the contact area. This increase in contact area results in a displacement of material away from the stick zone along the x-axis (and z-axis) due to the Poisson effect. The resulting roller displacement is represented in red in Fig. 2 (b). Similarly, Fig. 2 (c) presents the resulting normalized z-component of displacement (w) and Fig. 2 (d) provides a simplified model for this deformation. As contact area increases, regions of the roller on the edge of the stick zone press out along the z-axis due to the Poisson effect. For both Figs. 2 (a) and (c) there is no displacement in the middle of the tire due to symmetry of loading and geometry. However, differing from Fig. 2 (a), the displacement is localized to regions adjacent to the stick zone area and does not disperse through the rest of the roller. Figures 2 (e) and (f) present the sidewall displacement fields. These fields are consistent with classical Hertz theory as the y-component of deformation (v) is elliptical around the contact area and both u and v are symmetric about the axis of compression. These results are also consistent with Ref. [45] which analyzes Hertzian contact between a cylindrical disk and a rigid surface. The experimentally obtained u displacement also agrees with Hertz theory due to the sidewall being split into two regions of positive and negative displacement.

Figure 3 presents the top and side view strain fields. Figures 3 (a) - (c) document the contact area strains produced using the displacement fields in Figs. 2 (a) and (c). Similarly, Figs. 3 (d) - (f) display the sidewall strains calculated using Figs. 2 (e) and (f).

Note that the top view strain fields in Figs. 3 (a) - (c) have been corrected to account for the geometric flattening effect of the roller against the substrate. This effect is discussed further in Appendix B and is found to be small such that the maximum change in strain is less than 13%. Figure 3 (a)

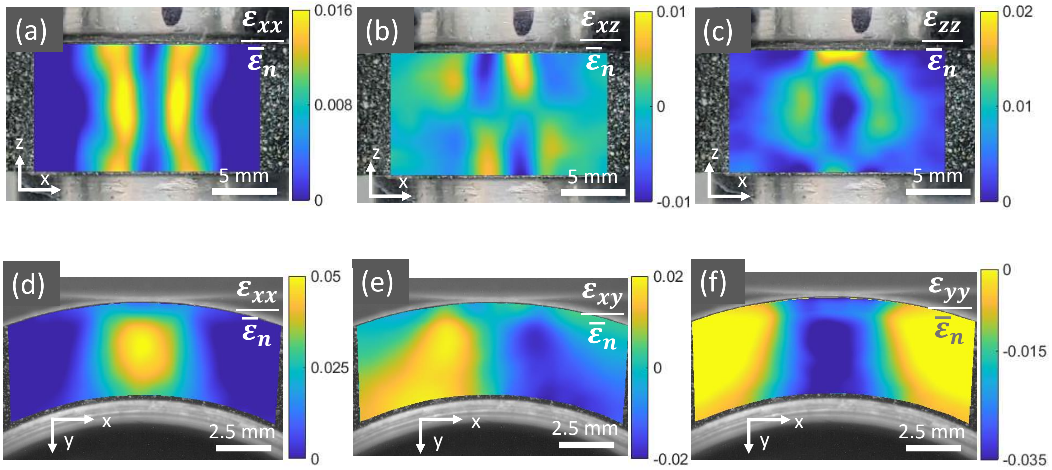

Figure 3: Strain fields of the roller under the applied normal load of N_{max} with respect to an undeformed roller and normalized with respect to $\bar{\varepsilon}_n$. Each strain field is an average of five trials. (a),(b),(c) - strain fields of the roller-substrate interface. (d),(e),(f) - strain fields of the roller sidewall.

displays the interface ε_{xx} field. The deformation is purely tensile as the roller deforms due to the y-direction normal load. Roller material displaces away from the center of the contact interface due to the Poisson effect. Strain ε_{xx} is close to zero near the vertical center-line of the contact interface, while ε_{xx} grows in magnitude as distance from the center-line increases. The strain reaches a maximum in two symmetric arcs of high strain outside of the contact patch where the roller surface is not constrained by frictional contact with the substrate.

Figure 3 (b) presents the ε_{xz} strain field which forms an antisymmetric pattern of alternating positive and negative zones of high strain. This strain pattern is more easily understood by returning to Fig. 2 (a) and (c) and applying the equation for shear strain,

$$\varepsilon_{xz} = \frac{1}{2}\left(\frac{\partial w}{\partial x} + \frac{\partial u}{\partial z} + \frac{\partial u}{\partial x}\frac{\partial u}{\partial z} + \frac{\partial w}{\partial x}\frac{\partial w}{\partial z}\right). \tag{1}$$

From Fig. 2 (a) we discern $\partial u/\partial z = 0$ and so only w affects the shear strain. Also, since the nonlinear terms are quadratic and strains are small, these terms are negligible reducing the shear strain to

$$\varepsilon_{xz} \approx \frac{1}{2}\left(\frac{\partial w}{\partial x}\right). \tag{2}$$

The regions of positive and negative $\partial w/\partial x$ are marked with positive and negative symbols in Fig. 2 (c) and match the shear strain regions in Fig. 3 (b). We note that a study of a soft cylindrical disk without an inner hub under normal loading in contact with a rigid substrate produced a very similar pattern of alternating positive and negative shear strain at the contact interface [25].

The ε_{zz} strain field in Fig. 3 (c) shows purely tensile strain similar to the ε_{xx} field in Fig. 3 (a). The strain at the center of the contact patch away from the edges of the roller is close to zero. Strain grows axially and circumferentially away from the center of the contact patch under normal loading due to the Poisson effect. Two zones with the highest magnitude strain form at the sidewall edges of the roller where no additional roller material constrains w. The non-constrained regions seen at the corners of the analyzed zone feature near-zero strain, as expected.

The ε_{xx} strain field of the roller sidewall shown in Fig. 3 (d) features a single high-strain zone directly below the contact interface. This strain field shows purely tensile normal strain. The roller section shown is compressed from both sides by the substrate and the hub, and roller material displaces away from the center-line of the contact interface while being constrained by the contact. The highest-magnitude strain is reached at the center of the roller. Strain far away from the center of the contact patch is nearly zero.

Figure 3 (e) displays the ε_{xy} strain field. Two anti-symmetric zones of high strain form on either side of the contact center-line where shear strain is zero. The shearing is induced by the Poisson effect where the roller material deforms away in the x-direction due to the compression of the roller by the substrate and roller hub. The shearing induced by the roller-hub contact appears to dominate the strain field as indicated by the large positive shear strain zone to the left and the large negative shear strain zone to the right of the contact center-line.

The ε_{yy} strain field in Fig. 3 (f) is purely compressive. The highest magnitude strain is directly below the center line of the roller-substrate interface. The magnitude of strain as well as the general shape of the high-strain zone do not change significantly along the y-direction. Strain decreases symmetrically about the y-axis center line below the contact point and reaches near-zero values away from the contact interface.

The sidewall strain fields in Figs. 3 (d) and (f) are symmetric about the axis of compression (y-axis) for ε_{xx} and ε_{yy}, while the shear strain in Fig. 3 (e) is anti-symmetric. These results are consistent with Ref. [45] and Hertzian contact between a cylinder and plane. These strain fields are

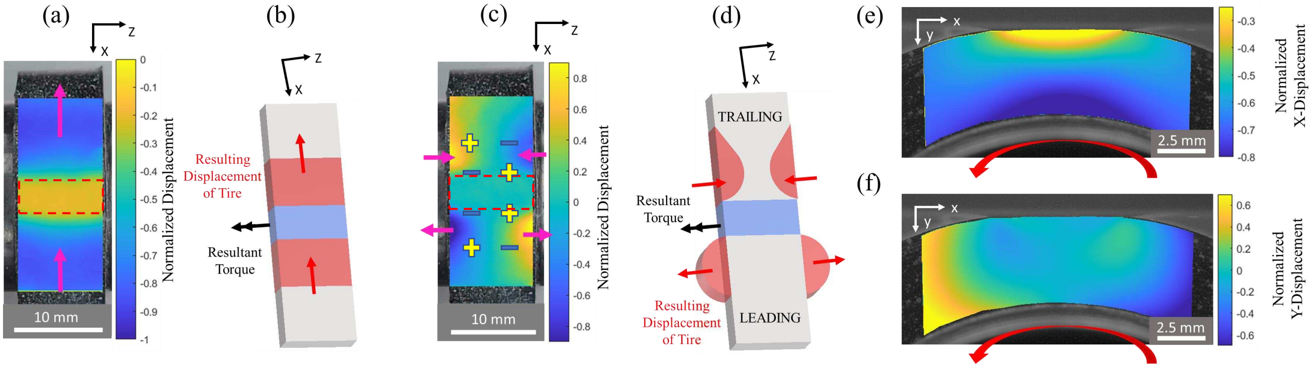

Figure 4: (a) Top view x-component of displacement resulting from a tangential load. The contact area is noted as a red dashed outline. (b) Simplified depiction of the u displacement field. The double arrows represent the resultant torque, the blue material represents the contact area, and the red regions represent the deformed roller material on either side of the contact area. (c) Top view z-component of displacement resulting from a tangential load. The positive and negative slopes ($\partial w/\partial x$) are marked with "+" and "-" signs respectively. (d) Simplified depiction for explaining the w displacement field. Material along the trailing edge thins while material along the leading edge accumulates. (e) Normalized sidewall u displacement resulting from a resultant torque. (f) Normalized sidewall v displacement induced by a resultant torque.

also very similar to the fields generated by the analytical thin layer approximate solution provided by Ref. [9], and the Hertzian contact solution provided by Ref. [10], both of which are presented in Appendix A. The experimental strain fields deviate from the analytical model near the roller-plane and roller-hub interfaces. In the thin layer approximation this is likely due to the presence of friction that are lacking in the analytical model while the Hertzian solution does not take into account the rigid hub. The experimental strain fields are consistent and repeatable between trials, which is demonstrated in the standard deviation fields in Appendix C. Note the locations of largest deviation appear mainly on the borders of the contact zone. This may be due to small fluctuations in establishing contact between trials. The strain fields also remain self similar with an increasing normal load (observed but not documented here).

4. Tangential Loading Under Constant Normal Load

Figure 4 (a) displays the top view of the experimentally obtained u displacement resulting from a tangential load inducing a torque. All displacements are measured relative to the reference configuration corresponding to N_{max}. It is expected from previous literature and proven later on in this work that the tangential load introduces regions of microslip in the contact area of the roller and substrate separating the contact area into stick and slip zones. The roller material outside of the contact area stretches in response to the applied load attempting to rotate counterclockwise. Figure 4 (b) depicts this resulting displacement field. As before, the blue section represents the contact area while the red sections represent the deformed roller material as a result of the induced torque. Figure 4 (c) documents the w displacement and is visualized using the depiction in Fig. 4 (d). Figure 4 (d) also marks the leading and trailing edges of the contact area which, when viewing the sidewall images, are the right and left edges, respectively. As the roller material is stretched in the trailing edge, it thins and as material is compressed against the leading edge of the contact area, material accumulates with increasing tangential load. This accumulation of material results in an outward displacement along the z-axis due to the Poisson effect. Similar to Fig. 2 (c), the z-component of displacement resulting from the torque is localized on the edges of the contact area. The contact area experiences minimal displacement since the majority of the area remains a stick zone.

Figures 4 (e) and (f) display the normalized sidewall v and u displacements, respectively. As expected, the material near the edges of the region of interest experiences deformation consistent with a roller rotating counterclockwise. Interestingly, two regions develop in the middle of the tire thickness that experience opposite y-components of displacement than the material around them. This is linked to the z-component of displacement described in Figs. 4 (c) and (d) with material accumulation along the leading edge and material thinning in the trailing edge. As material accumulates along the leading edge of the contact region its v displacement is constrained by the substrate so it presses some material downwards. Similarly, as the material thins along the trailing edge, it pulls some material beneath it upwards due to the Poisson effect. The x-component of displacement is also consistent with that expected. The material in contact with the glass substrate sticks and experiences minimal displacement due to the friction along the contact. However, due to the elastic nature of the roller, the material attached to the hub and the material around it experience negative x-components of displacement as the roller attempts to roll counterclockwise.

Figure 5 presents the strain fields resulting from induced torque. Figures 5 (a) - (c) document the top view strain fields produced using the displacement fields in Figs. 4 (a)

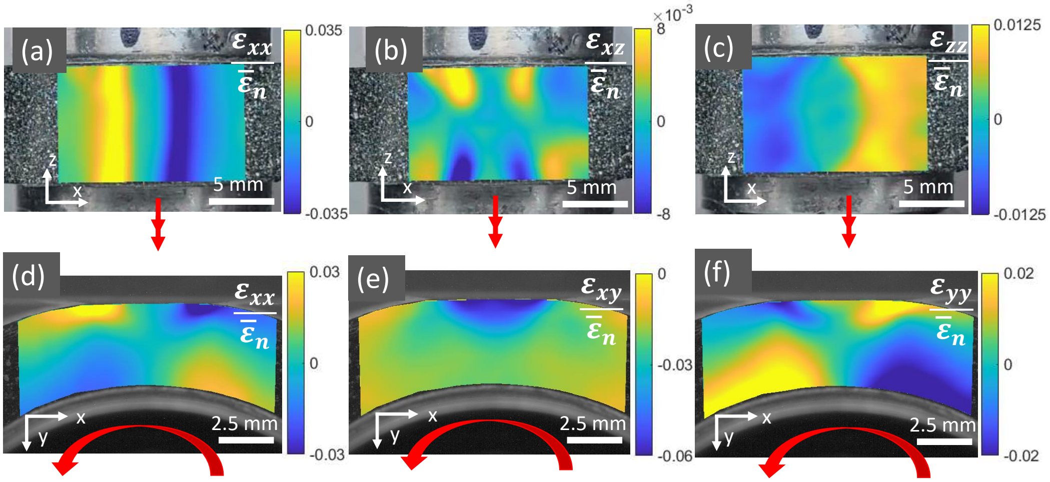

Figure 5: Normalized strain fields of the roller under the applied tangential hub load of T_{max} with respect to the roller under a N_{max} normal load. Each field is an average of 5 trials. (a),(b),(c) - strain fields of the roller-substrate interface. (d),(e),(f) - strain fields of the roller sidewall.

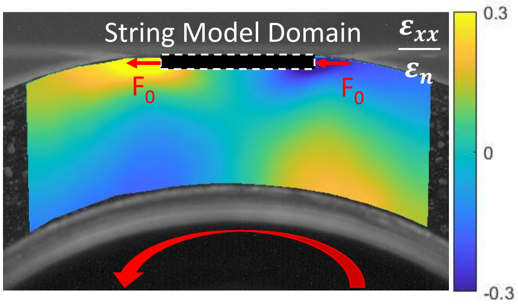

Figure 6: The string model domain representing the roller material in contact with the substrate. The horizontal tractions, F_0, acting on the ends of the string are induced by the counterclockwise torque.

and (c), while Figs. 5 (d) - (f) document the sidewall strain fields created using Figs. 4 (e) and (f). Similar to the strain fields resulting from normal loading, these strain fields are consistent and repeatable between trials, as displayed in the standard deviation fields in Appendix C, while also remaining self-similar with increasing resulting torque. Increasing the applied tangential load only increases the magnitude of the strain fields and decreases the stick zone. Unlike the strain fields resulting from normal loading, the geometric flattening effect of the roller against the substrate does not need to be taken into account for these top view strain fields. I.e., since the tangential loading strain fields are all measured relative to a reference configuration under normal load N_{max}, we expect negligible changes in the vertical displacement of the roller's hub and thus predict no further flattening.

In the ε_{xx} strain field in Fig. 5 (a), two distinct strain zones of opposite signs develop from the left and right sides of the contact interface. As the roller deforms under counterclockwise torque, the leading section, where material deforms toward the contact interface, is compressed, and the back section, where material deforms away from the contact interface, is stretched in the x-direction. Strain in the middle of the contact interface between the two zones is close to zero.

Figure 5 (b) features the interface ε_{xz} strain field. Similar to Fig. 3 (b), the shear strain field is best understood using Eq. (2). The regions of increasing and decreasing $\partial w/\partial x$ are marked with positive and negative symbols in Fig. 4 (c) which align with the experimentally obtained shear strain fields. Differing from the normal load shear strain in Fig. 3 (b), the edges of the contact region experience positive shear strain on one side of the roller sidewall and negative on the other sidewall.

Figure 5 (c) shows the ε_{zz} strain field at the interface. There are two distinct zones of strain on the leading and trailing edges of the roller. The front edge experiences tensile strain while the back edge experiences compressive strain in the z-direction. As the material along the leading edge is compressed in the x-direction, it expands in the z-direction and vice-versa in the trailing edge. The ε_{zz} strain field resembles the ε_{xx} strain field in Fig. 5 (a) with opposite signs. The ε_{zz} strain zones converge to almost touching near the sidewall edges of the roller compared to the ε_{xx} strain zones as there is no material there to resist z-direction deformation.

Figure 5 (d) shows the development of four distinct strain zones in the roller which form antisymmetric ε_{xx} strain fields. The four zones are situated at the leading and trailing edges of the roller-substrate interface and two more exist near the roller-hub interface. The material near the trailing edge is stretched as it is pulled away from the substrate, and the material in front of the contact area is compressed as it is pressed against the substrate. At the roller-hub interface, the opposite effect occurs and the material below the leading edge experiences tension while the material below the trailing edge experiences compression along the x-axis.

The ε_{xy} strain field in Fig. 5 (e) features purely negative shear strain throughout the roller sidewall. A small zone

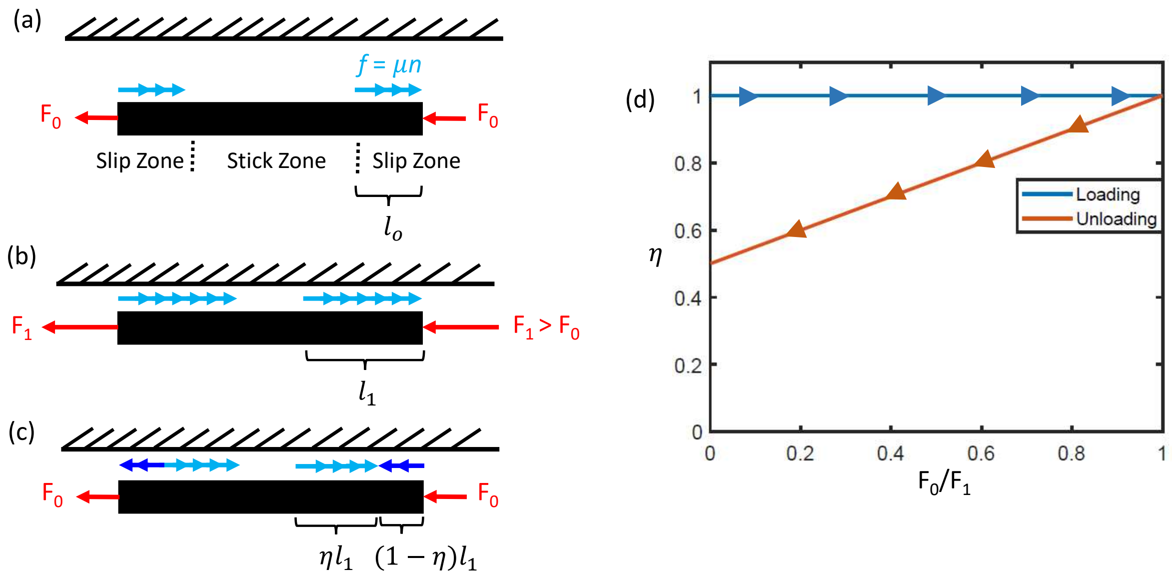

Figure 7: String model for contact region of an elastomer roller under counterclockwise torque illustrating memory upon load reversal. The string is assumed to experience an applied normal load of n per unit length (not depicted), resulting in a friction force per unit length μn under sliding conditions. (a) Small torque condition with associated horizontal loads F_0. A center stick zone emerges sandwiched between two slip zones, each of length l_0. (b) Large torque condition resulting in increased slip zone length l_1. (c) Return to small torque condition and depiction of partially reversed friction forces. η represents the fraction of slip zone length experiencing friction forces directed to the right. (d) Depiction of η during loading and unloading.

with the smallest magnitude shear strain develops directly below the roller-substrate interface. Two slightly negative zones form below the leading and trailing edges of the roller midway through the tire thickness. Unlike for the normal strain fields, no significant strain zones develop at the roller-hub interface.

Figure 5 (f) presents the sidewall ε_{yy} strain field. This field is a near-perfect mirror image of the ε_{xx} strain field in Fig. 5 (d). This is consistent with the mirroring interface ε_{xx} and ε_{zz} strain fields from Figs. 5 (a) and (c). The general shape of the strain field features and their magnitudes are similar, but the signs are opposite. The two zones developed at the roller-hub interface dominate the strain field similar to that observed in Fig. 5 (d). Smaller zones of tensile and compressive strain in the leading and trailing edges, respectively, develop at the roller-substrate interface. As the roller deforms due to the counterclockwise tangential load, the material at the roller-hub interface experiences compression below the leading edge and tension below the trailing edge.

5. Memory Effect

We next present analysis of a memory effect observed for impending slip, which we describe using a conceptual string model. We first emphasize that this string model is a conceptual model for explaining the development of stick and slip zones within the contact area as well as demonstrating how memory effects arise under cyclic loading. The values we calculate using this model are examples and do not capture with complete accuracy the state of contact in the experimental fields. The model captures deformation and frictional contact mechanics using a one-dimensional representation of a portion of the roller spanning the contact region, as depicted in Figure 6. Applied tractions, F_0, are induced by the counterclockwise torque and act on the ends of the string. Figure 7 (a) presents the string in isolation, including friction forces arising in the contact region. The string experiences an applied normal load of magnitude n per unit length (not pictured) resulting from the applied normal load N_{max} used in the experiment. We envision the interface between the string and substrate to be characterised by a coefficient of friction, μ, such that any fully developed friction has magnitude $f = \mu n$ per unit length. Being conceptual, we do not relate the model parameters (e.g., n, f, and μ) to the actual loading and roller parameters (e.g., N, T, and various geometrical parameters).

The elasticity of the string causes strain to develop in response to quasistatic loading F_0, resulting in slip at either end of the string as depicted in Fig. 7 (a). In these slip zones exist fully-developed friction forces opposing the deformation. Note that it is necessary for strain to develop only at the ends of the elastic string (i.e., the extremities of the contact region) rather than in the interior, as we substantiate using a consistency argument. If strain were to first develop from the center (or, similarly, anywhere else in the interior) of the string, these strains would result in rigid body motion of the string away from the center, which in turn would lead to fully developed friction forces along the entire upper surface of the string, the resultant of which would exceed the applied traction forces. Thus only strains originating at the ends is consistent with the model's kinematic assumptions and the

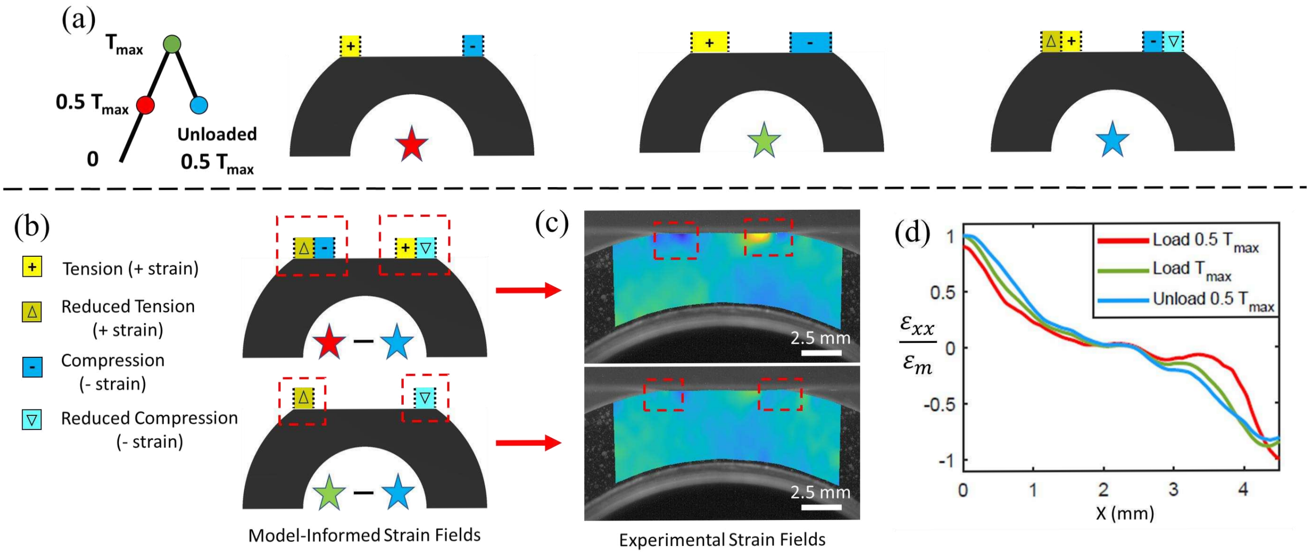

Figure 8: (a) Applied tangential loading path and illustrated ε_{xx} strain field in the contact region at each load. The illustrated strain fields represent strain fields normalized with their respective maximum and utilize colored boxes to represent strain where the colors follow the legend in subfigure (b). The strain colors are chosen to correlate with the strain field in Fig. 5 (d). The colored star in each subfigure represents the illustrated strain field resulting from the tangential loading represented by the matching colored circle on the tangential loading path. (b) Differences between illustrated strain fields. (c) Difference between experimentally measured strain fields. The strain fields correlate with those in (b) and are also normalized. (d) Comparison between the experimental strain along the contact edge for each loading case. X = 0 relates to the trailing edge of the contact region.

force balance requirement. Away from the slip zones, in the stick zone, the string experiences no friction forces. As depicted in Fig. 7 (b), if the applied end tractions increase quasistatically from F_0 to F_1, the length of the slip zones increase accordingly to maintain equilibrium, and thus the stick zone shrinks.

Interestingly, if the load is next reduced back to F_0, a memory effect sets in as depicted in Fig. 7 (c). The string model does not return to the friction state in Fig. 7 (a) due to friction at the ends of the string reversing direction to oppose the string relaxation. However, the sum of the original and reversed friction forces along l_1 must equate to F_0 in order to maintain equilibrium. We calculate the fraction of friction that is preserved using a force balance applied to both Figs. 7 (a) and (c),

$$F_0 = f l_0 = \eta(f l_1) - (1-\eta)(f l_1), \tag{3}$$

where η denotes the fraction of the slip zone in Fig. 7 (c) that experiences the preserved friction direction, l_0 denotes the slip zone length in Fig. 7 (a), and l_1 denotes the slip zone length in Fig. 7 (b). Rearranging Eq. (3) for η yields,

$$\eta = \frac{l_0 + l_1}{2l_1} = \frac{F_0 + F_1}{2F_1}, \tag{4}$$

where we have used l_0 and l_1 proportional to F_0 and F_1, respectively. Figure 7 (d) presents a trend from this memory effect illustrating the dependence of η on the loading history. During unloading, a percentage of l_1 is retained with a friction force direction originating from loading. When the horizontal traction is reduced to zero, half of the originally-generated friction forces persist (i.e., $\eta = 0.5$). Due to this memory effect, the strain fields experimentally measured can be expected to be hysteretic and dependent on loading history.

We verify the existence of this memory behavior experimentally by tracking the strain fields on the roller sidewall during increasing, and then decreasing, tangential load. Figure 8 (a) presents the loading and unloading map (left subfigure) as well as string model-informed predictions of ε_{xx} at each load (three right subfigures). The colors used in the illustrated predictions are based on those from the loading state in Fig. 5 (d) where the trailing region experiences tension (yellow) and the leading edge experiences compression (blue), resulting in positive and negative ε_{xx}, respectively. The illustrations represent strain fields normalized with their respective maximum to directly compare between $0.5\mathrm{T}_{max}$ and T_{max} fields. Note that the three illustrated strain predictions correlate to the string model states in Figs. 7 (a) - (c) and will be verified using Figs. 8 (c) and (d).

In the experiment, we first increase the tangential load from zero to $0.5\mathrm{T}_{max}$. Based on the prediction in Fig. 7 (a), we expect slip zones to form on either ends of the contact region. As we then increase the tangential load to T_{max}, the tension and compression regions are expected to grow accordingly (as in Fig. 7 (b)). After we then decrease the tangential load to $0.5\mathrm{T}_{max}$, due to the memory effect, we do not expect the roller to return to its original strain state. Instead, the roller is expected to experience only a reduction of tension and compression in the outermost strain

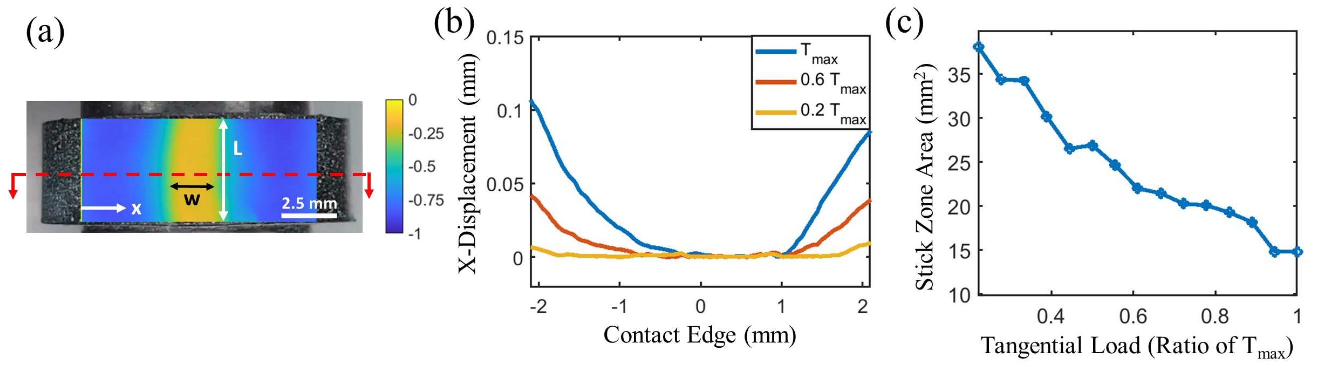

Figure 9: Tracking stick zone area with increasing tangential load. (a) The x-axis displacement field in the contact region. The stick zone is the rectangular zero displacement region defined as the area w × L. (b) The displacements along the red dashed line in (a) for three increasing tangential loads. The stick zone width (w) is measured as the distance the x-displacement is essentially zero. (c) The calculated stick zone area for increasing tangential loading between $0.2T_{max}$ and T_{max}.

regions (as predicted by Fig. 7 (c)). This progression is also illustrated using expected strains in the three subfigures to the right of the loading path in Figure 8 (a).

To highlight the differences between any two illustrated strain fields, we subtract the two fields predicted by the string model. Figure 8 (b) documents the differences between illustrated ϵ_{xx} strain fields where the colored stars represent the strain fields at each loading case in Fig. 8 (a). Counterintuitively, we see the largest difference between the two $0.5T_{max}$ (loaded and unloaded) strain fields. The illustrated differences consist of alternating tension and compression regions on either edge of the contact region where the inner strain regions are larger in magnitude. This difference is due to the lengthening of the slip zones under an increased tangential load, followed by reduction in strain at the contact region ends during unloading. Conversely, the strain field difference displayed in the bottom figure between the T_{max} load and unloaded $0.5T_{max}$ load exhibits the least difference. This is due to the inner strain regions negating each other, leaving only outer strain regions of reduced magnitude. The resulting difference results in only one region of reduced tension and one region of reduced compression in the left and right edges of the contact region, respectively.

Figure 8 (c) documents the difference in experimentally-measured strain fields correlating to the illustrated strain fields in 8 (b), where each experimental strain field is normalized with respect to its maximum magnitude prior to taking the difference. The top figure displays the alternating tension and compression regions on both ends of the contact edge, consistent with the illustrated strain field. While the bottom experimental difference strain field does not display as strong agreement with the illustrations, it does support the conclusion that only small strains remain. The strain field differences throughout the loading history, and the failure of the strain field to return to its original sate after unloading, strongly support the existence of the proposed memory effect.

We next plot the experimental strain across the contact edge for each loading case. Figure 8 (d) presents the experimental strain in the roller just below the contact patch for each loading case, where X = 0 refers to the trailing edge of the contact region. Each strain curve is normalized with respect to its absolute maximum magnitude to directly compare between both $0.5T_{max}$ and T_{max} loads. As expected, the loaded $0.5T_{max}$ strain curve closely resembles the strain produced from the string model in Fig. 7 (a). The strain has a zero strain (stick) region in the middle while two non-zero strain (slip) regions develop on either ends of the contact edge. The T_{max} strain curve also agrees with the strain produced from the string model in Fig. 7 (b). The center of the contact region continues to experience a zero strain region, of smaller extent, followed by a rapid increase in strain magnitude in the slip zones as the edges of contact are reached. These slip zones are larger than those observed for the loaded $0.5T_{max}$ curve, as expected from the model. Also as expected, we see the unloaded $0.5T_{max}$ curve more closely resembling the loaded T_{max} curve. The unloaded $0.5T_{max}$ curve experiences a zero strain region in the center of the contact edge similar to the other curves, but also experiences large slip regions at either end of the contact edge, differentiating it from the loaded $0.5T_{max}$ curve.

6. Stick Zone

Lastly, we introduce a method using DIC to measure the stick zone area of the roller under increasing tangential loading. We expect from previous theoretical works as well as from the conceptual string model in Fig. 7 (b) that as the horizontal tractions increase, the slip zones grow and the stick zone shrinks. We verify this behavior experimentally using the x-axis displacement fields from Fig. 4 (a) measured at increasing tangential loads. The rectangular zero displacement section in Fig. 9 (a) is the stick zone for the roller under a tangential load of T_{max}. To obtain the stick zone width (w), we plot a single curve of the x-axis displacements along the red dashed line. Figure 9 (b) presents this curve for three tangential loads 0.2T$_{max}$, 0.6T$_{max}$, and T$_{max}$. The stick zone width is measured as the distance along the curve where the x-displacement is essentially zero (below 0.004 mm). Since the stick zone is rectangular, the contact width can be multiplied by the roller width (L) to obtain the rectangular stick zone area. It is readily apparent from Fig. 9 (b) that as the tangential load increases, the stick zone width, and thus area, decreases. We repeat this process for tangential loads between 0.2T$_{max}$ and T$_{max}$ in increments of 0.05T$_{max}$ and plot the resulting stick zone areas in Fig. 9 (c). The stick zone area continues to decrease as the tangential load increases until the gross slip occurs slightly beyond T$_{max}$. These experimental results support the predictions of the string model in Sec. 5 and are made possible by the full field of displacements measured by DIC.

7. Concluding Remarks

We have utilized DIC to measure the strain fields across an elastic roller's sidewall and contact area during both normal and tangential loading. The friction effects that are usually ignored in analytical models are readily apparent in the obtained strain fields near the roller-substrate and roller-hub interfaces. We have also demonstrated using a conceptual string model how stick and slip zones develop in the contact area during frictional pre-sliding problems. The same conceptual model was used to illustrate how a memory effect arises in the contact area resulting in residual deformation and strain during cyclic loading. Using the experimental displacement and strain fields, we measured the stick zone area and verified the existence of a memory effect within the contact area.

The presented strain fields assist in understanding the distribution of deformation throughout the roller and may assist with understanding roller contact instabilities and improve future roller designs. This work is also the first step towards implementing DIC in a dynamic rolling scenario where rolling instabilities, such as Schallamach waves may arise. Schallamach waves have been documented in belt drives by Wu *et al.* [2, 3], and due to the similarity with the system studied herein, are expected to arise in rolling of elastomer elements on rigid substrates. DIC imaging can be expected to provide valuable insight into the evolution of these instabilities and assist in understanding the mechanics involved in their generation during dyanamic rolling problems.

Acknowledgements

This material is based upon work supported by the National Science Foundation under Grant No. 1916840.

Appendix A Experimental Strain Normalization and Comparison to Theory

In this work, we normalize the amplitude of the experimental strain fields by dividing them by the average y-axis strain in the contact area of the roller and surface, $\bar{\varepsilon}_n$. The equations we present in this section are found in Ref. [9] by Popov. Figure 10 provides the contact model and variable definitions used in the following equations. To find $\bar{\varepsilon}_n$ we first calculate the total normal load in the contact area of the roller and substrate, which is found using

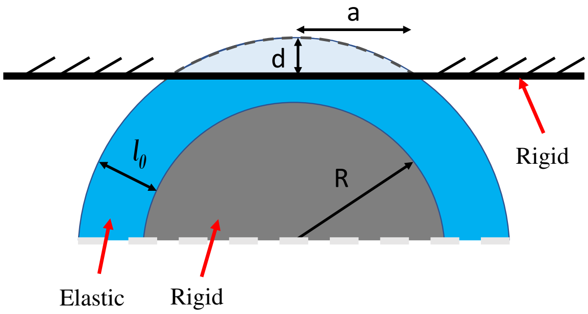

Figure 10: Roller-surface contact model for strain normalization. The roller variables are defined as follows: R represents the hub radius, d represents roller indentation depth, l_0 represents the roller thickness, and a represents the contact half width.

$$F = \frac{4}{3} 2^{1/2} \frac{\tilde{E} L R^{1/2} d^{3/2}}{l_0}, \tag{5}$$

where $\tilde{E}$ is the effective elastic modulus and L is the roller width. Figure 10 (a) defines R as the hub radius, d as the indentation depth, and l_0 as the roller thickness. The effective elastic modulus $\tilde{E}$ is calculated by

$$\tilde{E} = \frac{E(1-\upsilon)}{(1+\upsilon)(1-2\upsilon)}. \tag{6}$$

Next we calculate the contact area as a rectangle with area aL where a is the contact half width. The contact half width is often referred to as the radius of contact for spherical contact. We calculate a using

$$a = \sqrt{2Rd}. \tag{7}$$

From the contact force (F) and area (A), we calculate the stress to be F/A. This stress is converted to $\bar{\varepsilon}_n$ by multiplying it by the elastic modulus of the roller (E) leading to a normalization constant,

$$\bar{\varepsilon}_n = \frac{FE}{A}. \tag{8}$$

Figure 11 presents a comparison between the experimentally obtained strain fields (a - c) and the theoretical strain fields produced using both the thin layer approximation (d, e) and Hertzian cylindrical contact (f - h). The thin layer approximation is obtained from Ref. [9] pages 15 and 16 where Popov provides the equation for the y-axis strain of a thin elastic sheet on a rigid, cylindrical base in contact with a rigid plane relative to the cylinder. Reference [9] neglects frictional and adhesive effects while also assuming that the layer is 'thin' such that the elastic layer is significantly

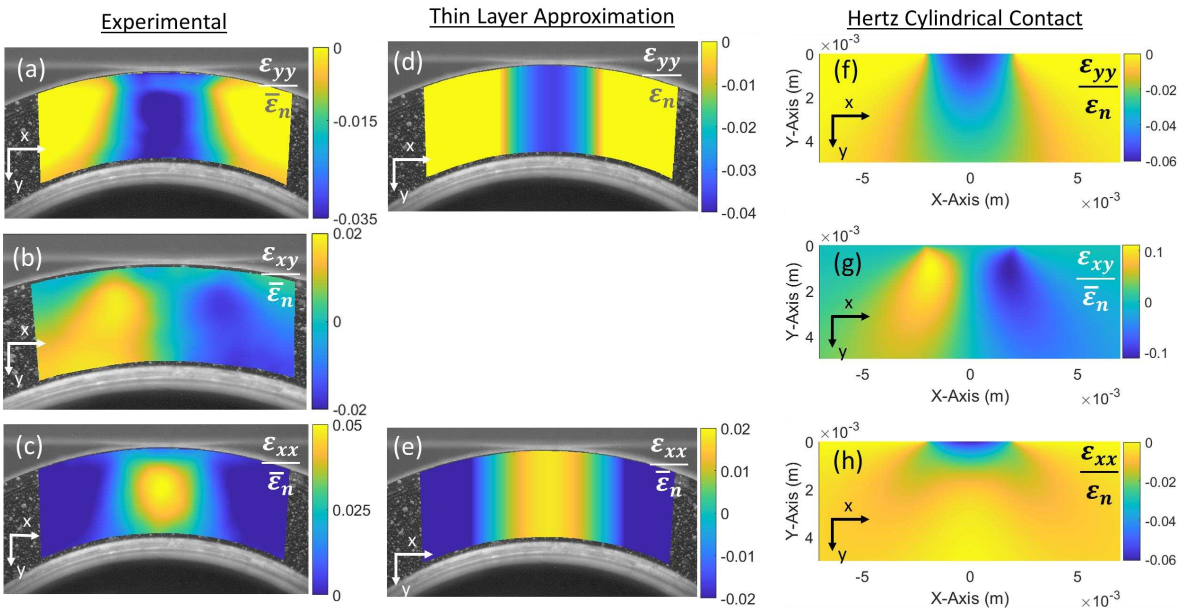

Figure 11: (a - c) Experimental strain fields for $\varepsilon_{yy}, \varepsilon_{xy}$, and ε_{xx} respectively. (d) and (e) Theoretical strain fields for ε_{yy} and ε_{xx}, respectively, using the thin layer approximation. (f - h) Theoretical strain fields for $\varepsilon_{yy}, \varepsilon_{xy}$, and ε_{xx} respectively using a Hertzian cylindrical contact model.

thinner than the length of the contact half width ($l_0 \ll a$) and the penetration depth much smaller than the elastic layer thickness ($d \ll l_0$). The penetration depth is indeed much smaller than the layer thickness ($d = 0.256$ mm $\ll l_0 = 5$ mm) but we acknowledge that the thickness of the elastic layer is not smaller than the contact half width ($l_0 = 5$ mm $\not\ll a = 2.1$ mm). However, we include the comparison here because it is one of the only analytical models that is applicable for comparison. The experimental strain fields we collect agree with this thin layer theoretical model while also demonstrating variation in strain inside the elastomer layer.

Since the experimental strain fields are relative to the undeformed substrate instead of the roller, we invert the sign of the theoretical strain field leading to

$$\varepsilon_{yy} = -\frac{d - x^2/2R}{l_0}. \tag{9}$$

Fig. 11 (d) presents the calculated theoretical ε_{yy} projected on the experimental roller. This theoretical strain field strongly agrees with the experimentally obtained ε_{yy} we present in Fig. 11 (a). Disparities between the two fields appear to be located at the contact region of the substrate and elastomer roller as well as between the elastomer roller and metal hub. This is likely due to the short contact half width as well as the frictional effect the theoretical model neglects.

We convert the theoretical ε_{yy} strain field to ε_{xx} by multiplying by the Poisson's ratio. Figure 11 (e) documents this theoretical ε_{xx} field. While the magnitude of the theoretical ε_{xx} field differs slightly from the experimental field in Fig. 11 (c), they strongly agree in orientation. Similar to the ε_{yy} fields, the discrepancies are located at the interface between the substrate and elastomer as well as elastomer and hub likely due to the short contact half width as well as the effect of friction.

The theoretical Hertzian contact model in Figs. 11 (f) - (h) is obtained from Ref. [10] where Johnson models the contact between two elastic cylinders using line loading of elastic half spaces. The Hertz theory assumes purely elastic bodies and neglects the contributions of the rigid cylindrical hub. It also maps the deformation within the elastic half space resulting from compression of a cylinder and not the deformation within the elastic cylinder itself. The equations for the resulting stresses in the half-space are obtained from Eq. 4.49 on pages 103 and 104 of Ref. [10] and are

$$\sigma_x = -\frac{p_0}{a}[m(1 + \frac{y^2 + n^2}{m^2 + n^2}) - 2y], \tag{10}$$

$$\sigma_y = -\frac{p_0}{a}m(1 - \frac{y^2 + n^2}{m^2 + n^2}), \tag{11}$$

and

$$\tau_{xy} = -\frac{p_0}{a}n(\frac{m^2 - y^2}{m^2 + n^2}) \tag{12}$$

where m and n are defined as

$$m^2 = \frac{1}{2}[((a^2 - x^2 + y^2)^2 + 4x^2y^2)^{1/2} + (a^2 - x^2 + y^2)] \tag{13}$$

and

$$n^2 = \frac{1}{2}[((a^2 - x^2 + y^2)^2 + 4x^2y^2)^{1/2} - (a^2 - x^2 + y^2)]. \tag{14}$$

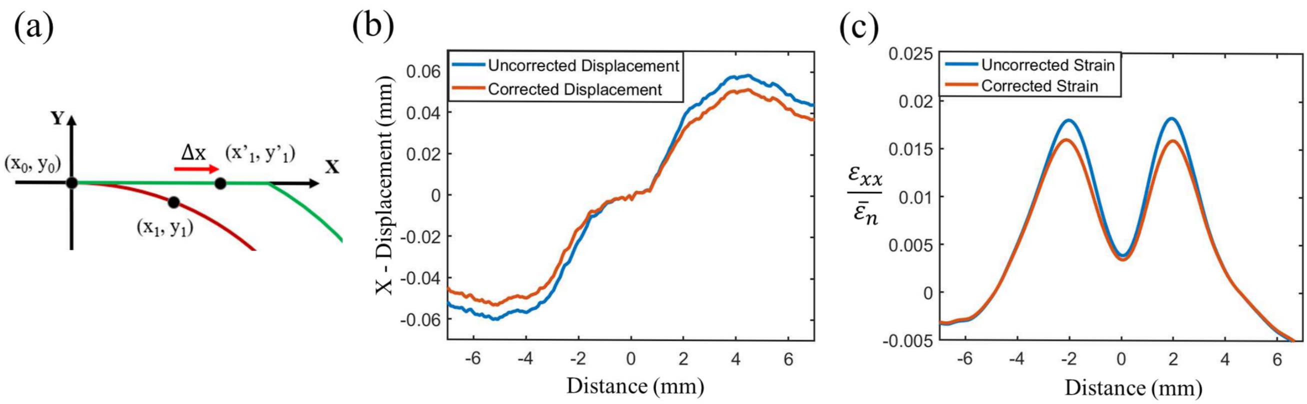

Figure 12: Adjusting DIC displacement and strain fields to account for roller flattening along the substrate. (a) As the roller comes into contact with the substrate, points along the roller will displace along the x-axis due to arc flattening. (b) The analytically calculated x-displacement due to flattening is subtracted from the experimentally obtained displacement. This process is done along the entire surface but is plotted along the red dashed line in Fig. 9 (a). (c) The strain fields are calculated using the updated displacements which only causes a small reduction in strain when compared to ignoring the flattening effect.

The signs of m and n are the same as the signs of y and x respectively. p_0 is the maximum pressure calculated from

$$p_0 = (\frac{PE}{\pi R})^{1/2} \tag{15}$$

where P is the load calculated using

$$P = \frac{\pi^2 E}{4R}. \tag{16}$$

Note in this case R is the radius of the roller ($l_0 + R$) and not the radius of the hub as presented in Fig. 10.

The resulting normal and shear stress fields are converted to strain fields by dividing them by the elastic modulus and shear modulus respectively. The resulting ε_{yy} and ε_{xy} fields in Figs. 11 (f) and (g) are very similar to the experimental fields in Figs. 11 (a) and (b). It is apparent that the rigid hub has significant effect on the strain fields that these Hertzian fields are missing but they still are fair initial approximations. The ε_{xx} field in Figs. 11 (h) is surprisingly inaccurate compared to the experimental field in Figs. 11 (c) with the resulting strain being negative and located at the contact point instead of positive at the midpoint of the elastomer layer. The location of maximum strain is again due to lacking the effects of the rigid hub. The sign of the ε_{xx} strain is likely since this is for the indented half space and not the indenting roller.

Appendix B Correcting For Roller Flattening

The top view strain fields resulting from purely normal loading (Figs. 3 (a) - (c)) are adjusted to take into account the geometric flattening effect of the roller as it is compressed against the substrate. As shown in Fig. 12 (a), points imaged prior to compression displace along the x-axis when the elastomeric roller flattens, even if the roller circumference is considered inextensible. Thus, imaging from the top in conjunction with DIC analysis would predict non-zero strain ε_{xx}. We correct these top view displacement fields to remove this flattening effect.

We know from optical measurements (not pictured) that a normal load of N_{max} results in a contact width of 4.2 mm. We analytically calculate the x-displacement of points along the roller circumference that result from compressing the roller enough to produce the measured contact width. Due to symmetry about the contact point, we only investigate one quarter of circumference as shown by Fig. 12 (a). The arclength from the origin to position x_j is equivalent to the x-location of the point after flattening and is found using the equation

$$x'_j = \int_0^{x_j} \sqrt{1 + (f'(x))^2}\,dx, \tag{17}$$

where $f(x)$ is the y-location of points along the roller circumference

$$f(x) = \sqrt{r^2 - x^2} - r, \tag{18}$$

and r is the radius of the roller (15 mm in this work). Equations 17 and 18 are combined and simplified to obtain the equation

$$x'_j = r \sin^{-1}\left(\frac{x_j}{r}\right). \tag{19}$$

Points within the contact region ($x'_j \leq 2.1$ mm) will relocate according to Eq. 19 while points outside the contact area will displace equally. The displacement at each point satisfies,

$$\Delta x_j = \begin{cases} r \sin^{-1}\left(\frac{x_j}{r}\right) - x_j & x_j \leq r \sin\left(\frac{2.1}{r}\right) \\ 2.1 - r \sin\left(\frac{2.1}{r}\right) & x_j > r \sin\left(\frac{2.1}{r}\right), \end{cases} \tag{20}$$

where $r \sin\left(\frac{2.1}{r}\right)$ is the x_j location corresponding to $x'_j =$ 2.1 mm. Note that after flattening, all points $x_j \geq r \sin\left(\frac{2.1}{r}\right)$

move rigidly with the displacement of the point associated with $x'_j = 2.1$ mm, as depicted in Fig. 12 (a).

Once we know the x-displacement due to flattening, we subtract it from the x-displacement field calculated using Ncorr. Figure 12 (c) displays the original and corrected displacement curves plotted along the red dashed line in Fig. 9 (a). As shown, the adjustment is very small. The adjusted x-displacement field along with the original y-displacement field are re-submitted to Ncorr which calculates the adjusted strain fields. As shown in Fig. 12 (d), the adjustment in strain fields is very small such that the maximum change in strain is less than 13% and the strain field does not change qualitatively. This difference in strain due to flattening is also comparable to the strain uncertainty. The peak strain in this loading scenario must overcome a noise floor before forming repeatable patterns. For this loading scenario the uncertainty is found to be approximately 0.005 for normally loaded ϵ_{xx}.

Appendix C Standard Deviation in multiple tests of the experimentally measured strain fields

Since the elastomeric roller is loaded and unloaded elastically, we expect to produce the same strain fields repeatedly. To demonstrate the consistency of the strain fields documented in Figs. 3 and 5, we present Figs. 13 and 14 which display the standard deviation fields of the five loading cases averaged to obtain the normal and tangentially loaded strain fields, respectively. The standard deviations between trials remain extremely small with a maximum of 0.0113 for normal loading and 0.0143 for tangential loading. There appears to be an edge effect due to the maximum standard deviations generally appear near the roller's outer edges. These larger standard deviations may be due to small geometrical inconsistencies in the roller edges around the circumference of the roller. One such example is a slightly raised lip on the roller outer edges which was slightly inconsistent along the circumference of the roller. While there are locations of higher standard deviations, the mean standard deviations across the strain fields remain below 30% of the mean strain except for the ϵ_{xz} and fields which have slightly larger mean standard deviation of approximately 55% of the mean strain. Overall the standard deviations fields support a repeatable strain field even though some areas near the contact edges experience some variation between trials.

References

[1] A Schallamach. How does rubber slide? *Wear*, 17(4):301–312, 1971.

[2] Yingdan Wu, Michael J Leamy, and Michael Varenberg. Schallamach waves in rolling: Belt drives. *Tribology International*, 119:354–358, 2018.

[3] Yingdan Wu, Michael Varenberg, and Michael J Leamy. Schallamach wave-induced instabilities in a belt-drive system. *Journal of Applied Mechanics*, 86(3):031002, 2019.

[4] C Cattaneo. Sul contatto di due corpi elasticie: distribution locale degli sforzi. *Reconditi dell Academia Nazionale die Lincei*, 27:474–478, 1938.

[5] Raymond David Mindlin. Compliance of elastic bodies in contact. 1949.

[6] Michele Ciavarella. The generalized cattaneo partial slip plane contact problem. i—theory. *International Journal of solids and structures*, 35(18):2349–2362, 1998.

[7] Michele Ciavarella. The generalized cattaneo partial slip plane contact problem. ii—examples. *International journal of solids and Structures*, 35(18):2363–2378, 1998.

[8] Heinrich Hertz. Ueber die berührung fester elastischer körper. 1882.

[9] Valentin L Popov et al. *Contact mechanics and friction*. Springer, 2010.

[10] Kenneth Langstreth Johnson. *Contact mechanics*. Cambridge university press, 1987.

[11] Hamid Ghaednia, Xianzhang Wang, Swarna Saha, Yang Xu, Aman Sharma, and Robert L Jackson. A review of elastic–plastic contact mechanics. *Applied Mechanics Reviews*, 69(6), 2017.

[12] LM Keer, N Ahmadi, and T Mura. Tangential loading of elastic bodies in contact. *Computers & Structures*, 19(1-2):93–101, 1984.

[13] V Brizmer, Y Kligerman, and I Etsion. The effect of contact conditions and material properties on the elasticity terminus of a spherical contact. *International journal of solids and structures*, 43(18-19):5736–5749, 2006.

[14] Xin Zhao and Zili Li. The solution of frictional wheel–rail rolling contact with a 3d transient finite element model: Validation and error analysis. *Wear*, 271(1-2):444–452, 2011.

[15] Marek Bijak-Żochowski and Piotr Marek. Residual stress in some elasto-plastic problems of rolling contact with friction. *International Journal of Mechanical Sciences*, 39(1):15–32, 1997.

[16] Chongfeng Wei. *A finite element based approach to characterising flexible ring tire (FTire) model for extended range of operating conditions*. PhD thesis, University of Birmingham, 2015.

[17] André Oliveira Köhn and Fernando De Azevedo Silva. A numerical and analytical study of the stress field generated by the contact between a rail and a wheel. *SN Applied Sciences*, 2:1–8, 2020.

[18] Dong-Hyong Lee, Jung-Won Seo, Seok-Jin Kwon, and Ha-Young Choi. Three-dimensional transient rolling contact analysis of similar elastic cylinders. *Procedia Engineering*, 10:2633–2638, 2011.

[19] J Blaber, B Adair, and Antonia Antoniou. Ncorr: open-source 2d digital image correlation matlab software. *Experimental Mechanics*, 55(6):1105–1122, 2015.

[20] Aakash Mange, Vanshaj Srivastava, Jess More, et al. Using digital image correlation to measure dynamics of rolling tires. Technical report, SAE Technical Paper, 2018.

[21] Chen Liang, Haowen Li, Hoda Mousavi, Guolin Wang, and Kangying Yu. Evaluation and improvement of tire rolling resistance and grip performance based on test and simulation. *Advances in Mechanical Engineering*, 12(12):1687814020981173, 2020.

[22] Ari J Tuononen. Digital image correlation to analyse stick–slip behaviour of tyre tread block. *Tribology International*, 69:70–76, 2014.

[23] Mehmet E Kartal, Daniel M Mulvihill, David Nowell, and David A Hills. Measurements of pressure and area dependent tangential contact stiffness between rough surfaces using digital image correlation. *Tribology International*, 44(10):1188–1198, 2011.

[24] KS Parel, RJ Paynter, and D Nowell. Linear relationship of normal and tangential contact stiffness with load. *Proceedings of the Royal Society A*, 476(2243):20200329, 2020.

[25] Thi-Lo Vu, Jonathan Barés, Serge Mora, and Saeid Nezamabadi. Deformation field in diametrically loaded soft cylinders. *Experimental Mechanics*, 59(4):453–467, 2019.

[26] Shengbo Eben Li, Hailiang Chen, Renjie Li, Zhengyu Liu, Zhitao Wang, and Zhe Xin. Predictive lateral control to stabilise highly automated vehicles at tire-road friction limits. *Vehicle system dynamics*, 58(5):768–786, 2020.

[27] Zhang Yanhui, Wang Zhijun, Li Xiaoping, and Wu Song. Research on the burst-tire car of direction instability of dynamic model based on load transfer. In *2010 International Conference on Optoelectronics and Image Processing*, volume 2, pages 281–284. IEEE, 2010.

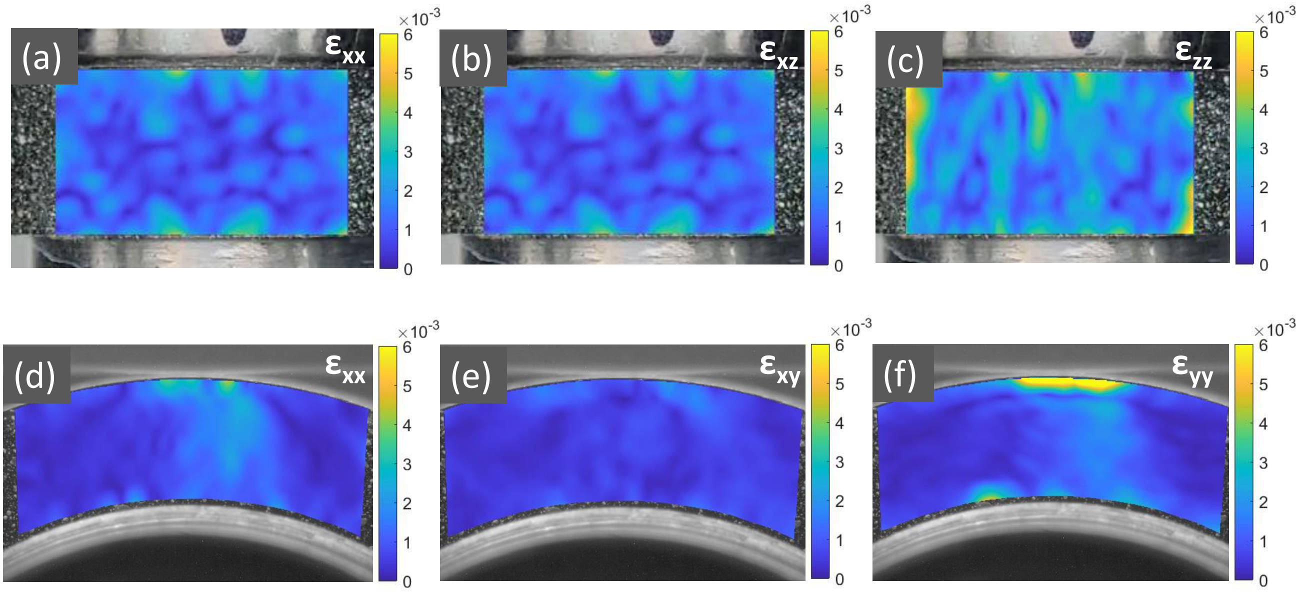

Figure 13: Standard deviation fields for five strain fields generated under normal loading averaged to generate Fig. 3.

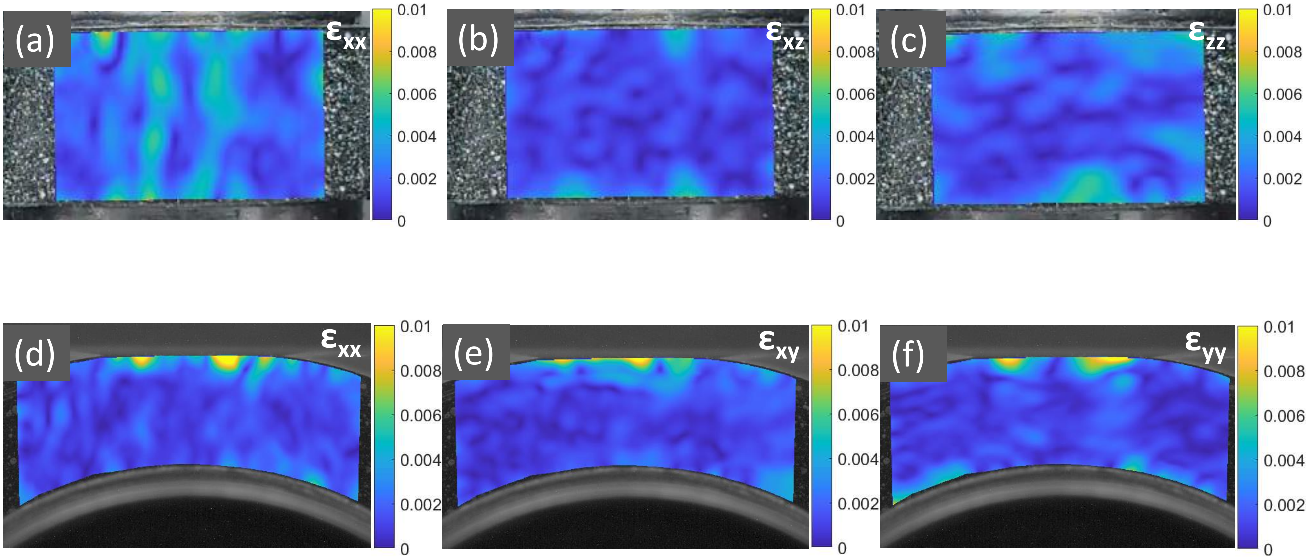

Figure 14: Standard deviation fields for five strain fields generated under tangential loading averaged to generate Fig. 5.

[28] J Jäger. A new principle in contact mechanics. 1998.

[29] JR Barber. Frictional systems subjected to oscillating loads. *Annals of Solid and Structural Mechanics*, 2:45–55, 2011.

[30] JR Barber and JR Barber. Rolling and sliding contact. *Contact Mechanics*, pages 433–473, 2018.

[31] James R Barber. Nominally static frictional contacts under periodic loading. *The Journal of Strain Analysis for Engineering Design*, 51(4):270–278, 2016.

[32] Young Ju Ahn, Enrico Bertocchi, and JR Barber. Shakedown of coupled two-dimensional discrete frictional systems. *Journal of the Mechanics and Physics of Solids*, 56(12):3433–3440, 2008.

[33] S Reina, D Dini, and DA Hills. Interfacial slip and creep in rolling contact incorporating a cylinder with an elastic layer. *European Journal of Mechanics-A/Solids*, 29(5):761–771, 2010.

[34] Bernhard Stingl, Michele Ciavarella, and Norbert Hoffmann. Frictional dissipation in elastically dissimilar oscillating hertzian contacts. *International Journal of Mechanical Sciences*, 72:55–62, 2013.

[35] Milosz K Rajchel, Michael Varenberg, Michael J Leamy, and Antonia Antoniou. Instrument for in situ study of rolling under normal load and torque. *Review of Scientific Instruments*, 93(9):093705, 2022.

[36] H Fromm, E Hoffman, R Harling, H Schrode, P Kraft, Franz Nikolaus Scheubel, E Maier, L Huber, TE Schunck, P Riekert, et al. Papers on shimmy and rolling behavior of landing gears presented at stuttgart conference october 16 and 17, 1941. Technical report, 1954.

[37] L Segel. Force and moment response of pneumatic tires to lateral motion inputs. 1966.

[38] J.Y. Wong. *Theory of Ground Vehicles*. Wiley, 2008.

[39] John C Dixon. *Tires, suspension and handling*. SAE international, 1996.

[40] James Lacombe. Tire model for simulations of vehicle motion on high and low friction road surfaces. In *2000 Winter Simulation Conference Proceedings (Cat. No. 00CH37165)*, volume 1, pages 1025–1034.

IEEE, 2000.

[41] Jacob Svendenius. *Tire modeling and friction estimation*. PhD thesis, Lund University, 2007.

[42] J Dundurs. Discussion:“edge-bonded dissimilar orthogonal elastic wedges under normal and shear loading”(bogy, db, 1968, asme j. appl. mech., 35, pp. 460–466). 1969.

[43] Farid H Benvidi and Mattia Bacca. Theoretical limits in detachment strength for axisymmetric bi-material adhesives. *Journal of Applied Mechanics*, 88(12):121007, 2021.

[44] Quy-Dong To and Q-C He. On the conforming contact problem in a reinforced pin-loaded structure with a non-zero second dundurs' constant. *International Journal of Solids and Structures*, 45(14-15):3935–3950, 2008.

[45] Serge Mora, Thi-Lo Vu, Jonathan Barés, and Saeid Nezamabadi. Highly deformed grain: from the hertz contact limitation to a new strain field description in 2d. In *EPJ Web of Conferences*, volume 140, page 05011. EDP Sciences, 2017.